COUPLED INVERSE MODELING OF A CONTROLLED IRRIGATION EXPERIMENT USING MULTIPLE HYDRO-GEOPHYSICAL DATA

Published version:

DOI:10.1016/j.advwatres.2015.03.008

Accepted Manuscript

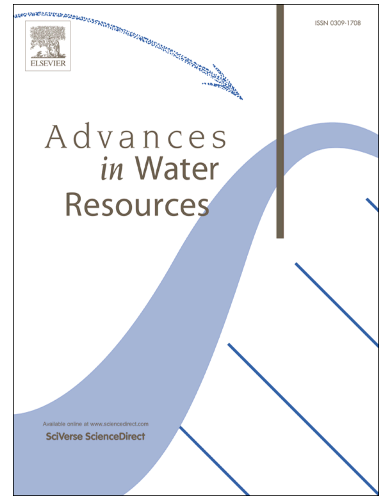

Coupled inverse modeling of a controlled irrigation experiment using multiple hydro-geophysical data

Matteo Rossi, Gabriele Manoli, Damiano Pasetto, Rita Deiana, Stefano Ferraris, Claudio Strobbia, Mario Putti, Giorgio Cassiani

PII:	S0309-1708(15)00063-9
DOI:	http://dx.doi.org/10.1016/j.advwatres.2015.03.008
Reference:	ADWR 2355
To appear in:	*Advances in Water Resources*
Received Date:	29 July 2014
Revised Date:	24 March 2015
Accepted Date:	25 March 2015

Please cite this article as: Rossi, M., Manoli, G., Pasetto, D., Deiana, R., Ferraris, S., Strobbia, C., Putti, M., Cassiani, G., Coupled inverse modeling of a controlled irrigation experiment using multiple hydro-geophysical data, *Advances in Water Resources* (2015), doi: http://dx.doi.org/10.1016/j.advwatres.2015.03.008

COUPLED INVERSE MODELING OF A CONTROLLED IRRIGATION EXPERIMENT USING MULTIPLE HYDRO-GEOPHYSICAL DATA

MatteoRossi[1], Gabriele Manoli[2], Damiano Pasetto[3],Rita Deiana[4], Stefano Ferraris[5], Claudio Strobbia[6], Mario Putti[3] and Giorgio Cassiani[1]

[1] Department of Geosciences, University of Padova, Via Gradenigo 6, 35131 Padova, Italy

[2] Nicholas School of the Environment, Division of Earth and Ocean Sciences, Duke University, Durham, North Carolina 27708, USA[3] Department of Mathematics, University of Padova, Via Trieste 63, 35121 Padova, Italy

[4] Department of Cultural Heritage, University of Padova, Piazza Capitaniato 7, 35139 Padova, Italy.

[5] Department of Agricultural, Forestry and Environmental Economics and Engineering, University of Torino, Via Leonardo da Vinci 44, 10095 Grugliasco, Torino, Italy

[6] Total SA, Pau, France

March 25, 2015

KEYPOINT: Comparison of hydro-geophysical inversion approaches applied to a surface irrigation experiment.

ABSTRACT

Geophysical surveys can provide useful, albeit indirect, information on vadose zone processes. However, the ability to provide a quantitative description of the subsurface hydrological phenomena requires to fully integrate geophysical data into hydrological modeling. Here, we describe a controlled infiltration experiment that was monitored using both electrical resistivity tomography (ERT) and ground-penetrating radar (GPR). The experimental site has a simple, well-characterized subsoil structure: the vadose zone is composed of aeolic sand with largely homogeneous and isotropic properties. In order to estimate the unknown soil hydraulic conductivity, we apply a data assimilation technique based on a sequential importance resampling (SIR) approach. The SIR approach allows a simple assimilation of either or both geophysical datasets taking into account the associated measurement uncertainties. We demonstrate that, compared to a simpler, uncoupled hydro-geophysical approach, the coupled data assimilation process provides a more reliable parameter estimation and better reproduces the evolution of the infiltrating water plume. The coupled procedure is indeed much superior to the uncoupled approach that suffers from the artifacts of the geophysical inversion step and produces severe mass balance errors. The combined assimilation of GPR and ERT data is then investigated, highlighting strengths and weaknesses of the two datasets. In the case at hand GPR energy propagates in form of a guided wave that, over time, shows different energy distribution between propagation modes as a consequence of the evolving thickness of the wet layer. We found that the GPR inversion procedure may

produce estimates on the depth of the infiltrating front that are not as informative as the ERT dataset.

KEYWORDS: hydro-geophysical inversion, electrical resistivity tomography, ground-penetrating radar, infiltration, vadose zone.

1. INTRODUCTION

Hydrological research increasingly requires detailed information to feed data-hungry numerical models. For this reason, geophysical data are increasingly called into play to fill the lack of spatial and sometimes temporal resolution of traditional hydrological data. This is particularly true for the vadose zone, where the difficulties for obtaining direct measurements, the general lack of knowledge and the uncertainty on the soil parameters and their spatial heterogeneity often lead to develop numerical models that cannot reproduce the behavior of the real systems, unless they are strongly constrained by multiple, extensive and complementary data.

The vadose/unsaturated zone is home to a number of complex key processes that control the mass and energy exchanges in the subsurface (soil water migration) and between the subsurface and the atmosphere (rain infiltration, soil evaporation and plant transpiration). The understanding of vadose zone fluid-dynamics is key to the comprehension of a large number of hydrologically-controlled environmental problems, with strong implications in water resources management and subsurface contaminant hydrology. Unsaturated processes are also key factors in a number of important issues, such as the availability of water for agriculture, slope stability, and floods. The dependence of the hydro-geophysical response on changes in soil moisture content is the key mechanism that allows the monitoring of the vadose zone in time-lapse mode via non-invasive techniques. The use of these techniques can provide high-resolution images of hydro-geological structures in the shallow and deep vadose zones and, in some cases, a detailed assessment of dynamical processes in the subsurface.

The estimation of the time and space variations of water content using non-invasive methodologies has been the focus of intensive research over the past three decades. Among the numerous techniques developed in literature for such a goal, such as electromagnetic induction, off-ground ground-penetrating radar, surface nuclear magnetic resonance, in this work we consider electrical resistivity tomography (ERT) and ground-penetrating radar (GPR). These techniques measure the electrical resistivity ρ (Ωm) and the relative dielectric permittivity ε_r (-) of the porous media, respectively. For both methods the determination of soil water content is based upon existing relationships that link water content to the geophysical quantities measured (e.g., Archie, 1942; Topp et al., 1980; Roth et al., 1990; Brovelli and Cassiani, 2008, 2011).

When used to study hydrological dynamics, GPR surveys are often performed to detect changes in soil moisture content via the variation of dielectric permittivity, generally measured from GPR travel times in a variety of configurations (e.g., Huisman et al., 2003; Cassiani et al., 2006; Cassiani et al., 2008), such as borehole-to-borehole (e.g., Rucker and Ferré, 2004a, 2004b; Rossi et al., 2012) or borehole-to-surface (e.g., Vignoli et al., 2012). However, the most common setup uses GPR antennas from the the ground surface, even though only few studies with this configuration have been focused on the understanding of the dynamics of the water front during irrigation (e.g., Galagedara et al., 2005; Moysey, 2010; Mangel et al., 2012; Lai et al., 2012) or using natural rainfall (Busch et al., 2014). When working solely from the ground surface, three approaches are possible to determine soil moisture content: (a) use the velocity of the direct ground wave, (b) estimating velocity from the reflected events, (c) estimating impedance and thus velocity from the reflected GPR signal. Approaches (a) and (b) share in fact the same operational characteristics, needing the two antennas to be separated from each other. Approach (c) does not require antenna separation and exploits the physics of the reflection mechanism, with its own advantages and disadvantages (e.g., Lambot et al., 2004; Schmelzbach et al., 2012), and with more limited applications so far. When the two antennas are separated from each other, the survey can be conducted in wide angle reflection and refraction (WARR) mode (e.g., van Overmeeren et al., 1997), where one antenna is kept fixed while the other is moved, or common mid point (CMP) (Fisher et al., 1992; Greaves et al., 1996; Steelman et al., 2012), where both antennas are moved simultaneously to keep the same mid-point. Both sounding techniques allow for a good identification of direct waves through the air and the ground. These methods are also employed for the estimation of velocity from the reflected events, even though for this use the normal move-out approach, typical of seismic processing, may not be ideal (see Becht et al., 2006 for a discussion). The estimation of velocity from the direct wave through the ground is the most widely adopted approach for vadose zone applications (e.g. van Overmeeren et al., 1997; Huisman et al., 2001; Hubbard et al., 2002). However, in some cases direct arrivals are not so straightforward to identify and can be confused with other events. This can happen in the presence of critically refracted radar waves (Bohidar and Hermance, 2002) or guided waves (Arcone et al., 2003; van der Kruk et al., 2006; Strobbia and Cassiani, 2007). A water front that infiltrates from the surface can give rise to such ambiguous situations, as the wet and consequently low velocity layer, lying on top of a faster (drier) media, can give rise to critically refracted waves (Bohidar and Hermance, 2002) as well as act as a waveguide confined between two faster layers: the air above and the drier media below (Strobbia and Cassiani, 2007), the two situations being defined by the ratio between the wavelength and the layer thickness. Therefore, to study infiltrating fronts, maximum care must be given in understanding the nature of the observed, multi-offset GPR signal, possibly exploiting the entire information content of the data (e.g. Busch et al., 2012).

ERT measurements (Binley and Kemna, 2005) have been widely employed to monitor water dynamics, as variations of moisture content (Daily et al., 1992; Binley et al., 1996) and salinity of pore water (Perri et al., 2012) leads to changes in the electrical properties of the media (La Brecque et al., 2004; Cassiani et al., 2009a). However, it is well known that resolution limitations (Day-Lewis et al., 2005) can produce severe mass balance errors (Singha and Gorelick, 2005) even in the most favorable cross-hole configurations. The problem is even more serious when only surface ERT are used to monitor natural or artificial irrigation from the ground surface (Michot et al., 2003; Clément et al., 2009; Caputo et al., 2012; Cassiani et al., 2012; Travelletti et al., 2012) where resolution dramatically drops with depth and a direct conversion of inverted resistivity values into estimates of soil moisture content may prove elusive.

Geophysical measurements can be informative of the hydrological response of the soil and subsoil if applied in time-lapse monitoring mode: some geophysical quantities (in this case, ρ and ε_r) are useful indicators of changes in the hydrological state variables, such as moisture content or pore water salinity. However, in order to extract this hydrological information, the assimilation of measurements in a hydrological model is needed. Two different approaches may be applied, named respectively "uncoupled" and "coupled" hydro-geophysical inversions (Ferré et al. 2009; Hinnell et al., 2010). The procedure for an *uncoupled inversion* can be summarized by the following steps:

1. the spatial distribution of the geophysical quantity of interest (e.g. electrical resistivity for ERT) is derived from the inversion of geophysical field data;
2. the application of a petro-physical relationship leads to obtaining, from the geophysical quantity, an estimation of moisture content distribution;
3. the estimated hydrologic state variable, in its spatio-temporal distribution, is used to calibrate and constrain a hydrological model, thus identifying the corresponding governing parameters.

The inversion of geophysical measurements is usually an ill-posed inversion problem that can be tackled introducing prior information. If no solid independent information is available, the most common approach is the introduction of a regularizing functional, commonly a smoothness constraint (Menke, 1984). As a consequence of ill-posedness and regularization, the inversion procedure can lead to artifacts, misinterpretations and unphysical results, especially in the subsurface regions where the sensitivity of the measurements is low (consider e.g. Day Lewis et al., 2005). To overcome these problems, a coupled hydro-geophysical modeling can be applied:

1. a hydrological model is used to predict the evolution of hydrological state variables – e.g. moisture content – on the basis of a set of hydrological governing parameters, the identification of which is the final aim of the inversion;
2. a suitable petrophysical relationship (same as for point (2) above) translates hydrological state variables into geophysical quantities, such as resistivity or dielectric permittivity;
3. the simulated geophysical quantities are used to predict the geophysical field measurements;
4. a comparison between predicted and measured geophysical field measurements allows a calibration of the complex of hydrological and geophysical models (thus the name "coupled inversion"), leading to the identification of the hydrological parameters, that is the key objective of the study.

In this work we follow a coupled approach within the framework of data assimilation (DA). DA schemes are mathematical tools of common use in hydrological applications. The main idea behind DA is using the field measurements to correct numerical simulations obtained with a hydrological model, thus modifying their governing parameters. This is possible by the recursion of forecast steps, which simulate the time-evolution of the probability density function (pdf) of the hydrological process, and analysis (or update) steps, which compute a posterior pdfs of the model parameters and state variables by assimilating the measurements (e.g., McLaughlin, 2002; Moradkhani et al., 2005). A few examples of coupled hydro-geophysical inversion exist in the literature (e.g., Busch et al., 2014) but the use of DA techniques is less widespread (Rings et al., 2010; Tran et al., 2014).

The present work focuses on a field experiment where artificial irrigation is monitored in time-lapse mode from the surface via both ERT and GPR. The homogeneous nature of the site, made of aeolic sand deposits, provides a simplified case study suitable to evaluate the performance of coupled hydro-geophysical inversion and test the information content of different geophysical data. Both GPR and ERT geophysical measurements are assimilated into the hydrological model CATHY (Camporese et al., 2010), that is employed for the numerical simulation of the experiment. We elected to use the iterative sequential importance resampling (SIR) proposed by Manoli et al. (2015) as a DA technique to estimate the model saturated hydraulic conductivity. This technique is particularly designed to assimilate geophysical measurements in a coupled hydro-geophysical model: the geophysical measurements are blended in the simulation to update the state of the system, estimate the model parameters and quantify the model uncertainties.

The specific goals of this work are:

1. to analyze in detail the nature of the WARR GPR data collected during the irrigation experiment, verifying whether or not complex refraction and waveguide phenomena occur during the progression of the wetting front, and how and to what extent this type of data can be processed and inverted;

2. to assess the effectiveness of incorporating ERT and GPR data in a coupled hydro-geophysical inversion procedure that, using the unsaturated flow equations, point directly at the estimation of the saturated hydraulic conductivity, and to compare this approach with the results of a classical uncoupled inversion approach;
3. to evaluate to what extent the information that can be obtained from GPR and ERT data corroborate each other, how the independent assimilation of each data type performs, if the assimilation of both geophysical techniques adds information with respect to separate procedures, and finally what is the value of using both techniques to monitor the infiltration process.

The paper is organized as follows: Section 2 is dedicated to the description of the hydrological model and the DA procedure used for the coupled inversion of the geophysical data. After presenting the hydrological experiment taken into consideration (Section 3), in Sections 4 and 5 we analyze the GPR and ERT data, respectively. In Section 6 we describe the setup for the DA procedure in this experiment. The benefits of the coupled inversion are presented in Section 7. The major conclusions of this work are summarized in Section 8.

2. DATA ASSIMILATION

Data Assimilation methods are typically made of three components: 1) a forward model describing the dynamics of the physical process under study, 2) an observation model that links the simulated system variables to the observed data, and 3) the update procedure, that changes the simulated variables on the basis of the observations. This section describes these three components for our particular

ACCEPTED MANUSCRIPT

application, i.e., the assimilation of ERT and GPR data to calibrate an unsaturated hydrological model with the iterative SIR method.

2.1 Hydrological model

The infiltration process in a variably-saturated isotropic porous medium is described by the Richards' equation:

$$S_s S_w(\psi)\frac{\partial \psi}{\partial t} + \phi \frac{\partial S_w(\psi)}{\partial t} = \vec{\nabla} \cdot \left[\boldsymbol{K_s} K_r(\psi)\left(\vec{\nabla}\psi + \eta_z\right)\right] + \mathrm{q} \tag{1}$$

where S_s is the elastic storage term [m^{-1}], S_w is water saturation [-], ψ is water pressure head/suction [m], t is time [s], ϕ is porosity [-], $\boldsymbol{K_s}$ is the saturated hydraulic conductivity [m s^{-1}] tensor, K_r is the relative hydraulic conductivity [-], $\eta_z = (0, 0, 1)^T$ with z the vertical coordinate directed upward, and q is a source/sink term [s^{-1}]. Eq. (1) is highly nonlinear due to the dependencies of soil saturation and relative hydraulic conductivity on pressure head. These terms are modeled using the water retention curves proposed by van Genuchten and Nielsen (1985).

2.2 Geoelectrical and GPR models for data assimilation

The electrical potential field induced in the soil by current injection during the ERT survey, Φ [V], can be modeled as:

$$-\vec{\nabla} \cdot \left[\rho^{-1}\vec{\nabla}\Phi\right] = I[\delta(\vec{r} - \vec{r}_{S+}) - \delta(\vec{r} - \vec{r}_{S-})] \tag{2}$$

where ρ is the electrical resistivity of the soil [Ωm], I is the applied current [A], δ is the Dirac function, $\vec{r} = (x, y, z)$, and $\vec{r}_{S+}$ and $\vec{r}_{S-}$ are the source and sink electrode positions, respectively. Here, the geophysical model is linked to the hydrologic model by the petrophysical relationship proposed by Archie (1942):

$$\rho(t_i) = \rho(t_0)\left(\frac{S_w(t_0)}{S_w(t_i)}\right)^n \tag{3}$$

where $S_w(t_0)$ is the background water saturation degree and $\rho(t_0)$ is the corresponding bulk electrical resistivity of the soil. In Eq. (2) the bulk electrical resistivity at i-th measurement time, $\rho(t_i)$, can be predicted by the knowledge of the saturation degree at the same time step, $S_w(t_i)$, and vice-versa. Thanks to Eqs. (2) and (3), we can write the ERT measurements, here indicated with $y_{\mathrm{ERT}}(t_i)$, as a nonlinear function H_{ERT} of the water saturation:

$$y_{\mathrm{ERT}}(t_i) = H_{ERT}\big(S_w(t_i)\big) + \nu_{ERT}(t_i) \tag{4}$$

where $\nu_{ERT}(t_i)$ represents a Gaussian measurement error with variance $R_{ERT}(t_i)$, $\nu_{ERT}(t_i) \sim N\big(0, R_{ERT}(t_i)\big)$.

For linking the GPR data to the hydrological model we adopt a simplified approach. The observation model that links the numerical simulations to the GPR measurements consists in the estimation of the infiltration front depth from the simulated vertical profiles of water saturation. When the considered porous media can be considered spatially uniform and the irrigation rate is nearly constant in time, at any assimilation time (t_1, t_2 or t_3) the water saturation can be considered uniform from the surface down to a certain depth d_1, while from d_1 to a depth d_2 it decreases to the initial saturation value according to the soil water retention curve, and finally the water content remains practically constant from d_2 to the bottom of the domain (considering that the water table is much deeper than the vertical extent of the infiltration domain). The average value of the two depths d_1 and d_2 is an approximation of the depth of the simulated infiltration front. Indicating the estimated infiltration front with $y_{\mathrm{GPR}}(t_i)$, from the described procedure we have that:

$$y_{\mathrm{GPR}}(t_i) = H_{GPR}\big(S_w(t_i)\big) + \nu_{GPR}(t_i) \tag{5}$$

where H_{GPR} is nonlinear operator and $\nu_{GPR}(t_i)$ is a Gaussian measurement error with with variance $R_{GPR}(t_i)$, $\nu_{GPR}(t_i) \sim N\big(0, R_{GPR}(t_i)\big)$. In the DA process $y_{\mathrm{GPR}}(t_i)$ is compared with the average thickness estimated from GPR measurements.

More accurate (and more complex) GPR modeling could be conducted to construct a forward model e.g. based upon a full-waveform approach (see e.g. Klotzsche et al., 2012, 2013). However we do not deem this is necessary for this case study, where the key information that is derived from GPR resides in the depth of the infiltration front and the electromagnetic (EM) wave propagation is dominated by guided waves (see Section 4).

2.3 Iterative SIR algorithm for Data Assimilation

In Manoli et al. (2015) the hydrological and geophysical models are coupled in a DA framework to simulate ERT surveys and update the physical state variable (soil saturation) and the model parameters whenever a geophysical measurement is available. DA methods allow the incorporation of real system observations onto the dynamical model to automatically correct the model forecast (i.e., the solution of Eq. 1) and the model parameters (e.g., the saturated hydraulic conductivity $\boldsymbol{K_s}$) thus reducing the uncertainties related to the model prediction. In the following we indicate with λ the set of time-independent model parameters in Eq. (1) and with $p_0(\lambda)$ its prior pdf.

The SIR algorithm uses a weighted Monte Carlo (MC) approach to perform the state and parameter update (e.g., Moradhkani et al., 2005). The MC realizations, which are also called particles, are initialized by sampling the parameter values from the prior distribution, $\left\{\lambda_0^j\right\}_{j=1}^N$, where N is the total number of MC realizations and j is the realization index. SIR associates a weight to each realization, w_0^j, which is initialized to $1/N$. The forecast step is given by the numerical solution of Richards's equation (1) for each set of parameters, thus describing the space and time evolution of the infiltration process. Note that weights and parameters are invariant during the forecast step. At a general time t, each realization is described by its particular set of parameters, state variables and weight $\left\{\lambda_t^j, S_w^j(t), w_t^j\right\}_{j=1}^N$.

In an assimilation step t_i, with the idea that the weight represent the 'closeness' of a realization to the real process, the SIR algorithm changes the weights according to the Bayes' formula: new weights are assigned to each particle on the basis of the likelihood function of the measured data with respect to the simulated data, e.g., $p(y_{ERT}(t_i)|S_w^j(t_i))$ for ERT data. The likelihood functions for the ERT and GPR data can be obtained from the measurement error pdfs described Eqs. 4 and 5, respectively. Then, the weights are changed with the following formula (here written for a general observation y):

$$\widetilde{w}_{t_i}^j = w_{t_{i-1}}^j p(y(t_i)|S_w^j(t_i)) \tag{6}$$

$$w_{t_i}^j = \frac{\widetilde{w}_{t_i}^j}{\sum_{j=1}^N \widetilde{w}_{t_i}^j} \tag{7}$$

where (7) is a normalization of the weights. Since some of the updated weights may be negligible, meaning that the corresponding particles are not representative of the physical process, the SIR introduces a resampling step after the update. In the resampling step, the particles with negligible weights are discarded, while those with large weights are duplicated, in order to retain only the particles that are more representative of the filtering probability. Manoli et al. (2015), similarly to Moradhkani et al. (2005), adapted this step to update also the model parameters: the weighted empirical distribution of the parameters is adopted to sample new parameter values the duplicated particles. The SIR method continues with a repetition of forecast and update steps, and terminates in correspondence of the last geophysical measurement. Since bias may be present in the initial model parameters, and since the hydraulic conductivity distribution may not converge during the sequential assimilation, the posterior distribution computed with the SIR method may not be optimal for the whole simulation. For this reason it is fundamental to iterate the described procedure until the parameter distribution is unchanged during the simulation. At each iteration the procedure initializes the parameters with an averaged posterior distribution, computed on the ensemble of the hydraulic conductivities computed after all the previous updates.

3. FIELD SITE AND IRRIGATION EXPERIMENT

The experimental site is located in the campus of the Agricultural Faculty of the University of Turin, Italy, in Grugliasco (45° 03' 52'' N, 7° 35' 34'' E, 290 m a.s.l.) (Fig.1). The depth of interest is the top 1 m from the ground surface, where the lithology is homogeneous. The stratigraphy is composed of a regular sequence of sandy soil (mesic Arenic Eutrudepts) and the sediments in this area are largely aeolic sands with extremely low organic content. The aeloic sand grains are relatively homogeneous in size with a mass median diameter (d_{50}) of about 200 μm and porosity ranging between 0.35 and 0.4 (Cassiani et al., 2009c). According to the Comprehensive Soil Classification System, the horizon down to about 1-1.5 meter depth is an A-horizon made of mineral matter (80% sand, 14% silt and 6% clay).

The water table is located around 20 m below the ground surface and therefore the shallow vadose zone, where our experiment took place, is not practically influenced by the underlying saturated zone. At the moment of the survey the vegetation was composed only of natural grass, no cultivation is present (Fig. 1b).

An infiltration experiment was performed at the site on August 28, 2009. The irrigation was provided by a 17 m line of sprayers. The soil surface covered by irrigation was approximately a rectangle of 18 m by 2.6 m (Fig. 1). The irrigation lasted for 5 hours and 45 minutes and was performed in 3 steps (Table 1), separated by intervals when a break of the irrigation allowed ERT and GPR acquisitions to be performed (see Fig. 1c for the geometry of the geophysical surveys). At the center of the ERT profile, along the sprinkler line, two Time Domain Reflectometry (TDR) probes were vertically placed in the soil with a length of 0.15 and 0.30 cm.

The irrigation intensity was always lower than the infiltration capacity of the soil, so no ponding was observed at the soil surface. The ERT and GPR measurements were performed with the schedule summarized in Table 2, where the time is referred to the starting of the irrigation.

4. GPR DATA ANALYSIS

The infiltration test was monitored by GPR using a PulseEkko Pro radar system (Sensors and Software Inc., Canada) with 100 MHz antennas. The surveys were repeated in time (Table 2) using a WARR scheme. The WARR profiles were acquired along the sprinkler line (Fig. 1c); the time sampling interval was 0.2 ns and the offset increment between transmitting and receiving antennas was equal to 0.1 m over a 10.5 m line, starting from an initial offset (minimal distance between transmitter and receiver) of 1 m.

The background WARR radargram before the irrigation is shown in Fig. 2, where we can clearly recognize the direct ground wave with a velocity of about 0.14 m/ns. The evolution of WARR surveys over time (Fig. 3) shows that the infiltration front modifies substantially the appearance of the GPR signal. The radargrams in Fig. 3 are distinctly different from each other: the direct radar wave in air is obviously unaltered over time, while the signal from the soil is progressively delayed. This phenomenon is due to the presence of a wet low-velocity layer, between the surface and the dry sandy soil, which becomes increasingly thicker over the irrigation period. At a first glance, the interpretation of the data may be conducted by identifying the first soil arrival as a critically refracted GPR wave that comes from the –wet - dry interface and arrives at larger intercept times as infiltration progresses, consistently with a deeper wetting front. Although, this event must be present in the data, it is likely to be masked by guided modes of GPR wave propagation as described by Strobbia and Cassiani (2007). The establishment of guided EM waves is the consequence of the geometry of the dielectric properties of the materials involved in the wave propagation. The energy radiated from the transmitting antenna is spread out into the low-velocity layer and reaches the underlying faster layer (dry sand) with an angle greater than the corresponding Snell critical angle, in such a way that the energy is totally reflected. The same phenomenon happens when the reflected energy reaches the boundary between the air and the wet sandy media. The total internal reflections guide the GPR waves horizontally inside the low-velocity layer, while outside of the wet layer there are only evanescent waves with no radiation in the dry material and in the air. A simpler interpretation of the radargrams (Fig. 3A) as a simple consequence of refracted events - albeit possible (see Cassiani et al., 2009b) - would lead to unclear event identification.

We analyzed the frequency-wavenumber (*f-k*) spectra of the radargrams with the aim of recognizing guided modes of wave propagation (Fig. 4A). The *f-k* spectra are obtained by a preprocessing involving several filtering procedures. The first preprocessing step consists in the application of a *de-wow* filter, following the procedure of Gerlitz et al. (1993). The *wow* effect is due to the air-ground pulse interference. In fact, electrostatic and inductive fields near the transmitter lead to the saturation of the receiver electronics and generate a low frequency contribution that decays with distance. The consequence of the *wow* is to move trace amplitude towards positive (or negative) values, resulting in a non-zero-mean trace. Removing the *wow* frequencies should reconstruct a zero-mean trace, where small amplitudes are easier to identify. This filter is based on the subtraction of the median amplitude, calculated inside a mobile window in the time domain. The window size is determined from the maximum *wow* frequency, achieved from the frequency spectra of all unfiltered traces (*f-x* spectra – i.e. one frequency spectrum for each offset x).

The second processing step is a *muting* of the portions of the radargram that are not relevant in the guided mode propagation, so as to highlight the signal of the supposed guided waves. The *muting* process has the aim of cleaning those portions of the radargrams that are not useful in the present study: events that may be considered as noise in a guided wave analysis. So *muting* is applied to remove the air direct wave as well as the reflected events at later times. We applied a Tukey window in time, to prevent ringing in the *f-k* domain that may be due to an abrupt signal step in the time domain. The Tukey window is set to obtain half of the entire window length as a flat plateau, while the two marginal sectors consist of segments of a phase-shifted cosine.

The final filtering process is the application of a finite impulse response (FIR) filter to remove signal noise at low and high frequencies. The FIR filter has a structure that can maintain the true intensity of the signal between 20 and 250 MHz. This is a broad window for a signal centered around 100 MHz, since the guided propagation shows apparent frequencies that can be higher than the acquisition capabilities of the receiving antenna. This fact is the consequence of the limitation of our array, that records the GPR echoes only at the ground surface.

The filtered radargrams are shown in Fig. 3B. The corresponding *f-k* spectra (Fig. 4A) show the signal evolution over time. The color scale of the power spectral density is the same for the different time-steps, in order to show the differences of energy distribution over time. The energy peaks at times t_1 and t_3 have much higher amplitudes than at time t_2, when energy peaks are relatively weak as energy is spread over several modes of propagation, while at times t_1 and t_3 a dominant mode is clearly recognizable. This may be the consequence of our spatial sampling that is not able to record with enough intensity the prevailing mode of resonance induced by that particular subsoil geometry, but can also be a symptom of the energy shifting between fundamental (at time t_1) and first higher mode (at time t_3). The positions of the absolute maxima, detected for each frequency, are plotted as magenta dots (Fig. 4A), while the white dots represent the local maxima.

Maxima picking in spectral amplitudes leads to obtaining the dispersion curves of Fig. 4B, showing the dependence of phase velocity on frequency. Here red dots correspond to the absolute maxima, while blue dots show local maxima. The dispersion curves at times t_1 show a clearly identifiable fundamental mode, while at time t_3 the first higher mode is much more energetic than the fundamental mode. The switch of the highest energy to higher modes of propagation may lead to the transient step which involves time t_2, where the power spectral density is spread upon different modes (Fig. 4A).

In order to give a hydrological meaning to these results, we need to translate the spectral analysis of guided waves into an estimate of the evolution of the hydraulic process. In particular we are interested in the location of the wetting front at depth, as this information is suitable for the calibration of hydrological models. The depth of this front corresponds to the thickness of the guiding high dielectric permittivity layer. The identification of the layer thickness and dielectric properties requires inversion of the dispersion curves (van der Kruk et al., 2006; Strobbia and Cassiani, 2007). We adopted as a forward model the description of the asymmetric slab waveguide given by Strobbia and Cassiani (2007). The approximation of 1-

ACCEPTED MANUSCRIPT

dimensional waveguide is valid as long as we assume that irrigation is practically uniform along the sprinklers' line, and the soil is largely homogeneous. The inversion of dispersion curves was performed using a MC approach. We sampled the controlling parameters, i.e.: velocity of the shallower wet layer, velocity of the deeper dry layer and thickness of the wet layer. The velocity of air can be considered a constant equal to 0.3 m/ns. To reduce the number of ensembles of parameters combinations, we fixed the value of the velocity of the deeper and faster layer to about 0.14 m/ns, i.e. we set it equal to the velocity of the soil before irrigation (Fig. 2). This choice is also in accordance with the TDR measurements (0.3 m prongs) performed before the irrigation, showing a dielectric permittivity of 4.55, which corresponds to a EM wave velocity of 0.141 m/ns. The forward model of EM wave propagation assumes the presence of only two ground layers, so we are not able to simulate a smoothed wetting front, that is approximated as a sharp discontinuity of dielectric permittivity. The thickness range is fixed, for all times, between 0.3 m and 1 m, with an increment of 0.05 m. The velocity of wet layer is sampled in the interval from 0.065 m/ns to 0.1 m/ns, at steps of 1.05×10^{-4} m/ns. Both fundamental and first modes are simulated, setting all possible combinations of the parameter space for a total of about 47000 simulations.

Fig. 5 shows the results of the inversion procedure, where the goodness of fit between experimental and simulated dispersion curves is calculated using the Nash-Sutcliffe index (NSI) (Nash and Sutcliffe, 1970). Fig. 5A reproduces the experimental curve (black dotted line) plotted together with the best-fitting synthetic curves: the light gray lines have NSI values between 0.85 and 0.95, while the dark gray lines show NSI>0.95. At time t_1 1035 curves of the fundamental mode have a NSI>0.95. At time t_2 the fitting of the measured dispersion curve for the fundamental mode is poor, as NSI does not exceed, for any curve, the value of 0.87. For this reason we consider in Fig. 5 only the 1124 simulations with NSI>0.85. The 1232 synthetic curves of the first higher mode are used to represent the experimental first mode at time t_3, where the NSI is greater than 0.95. We inverted the first higher mode for time t_3, as at this time the higher mode is much more energetic than the fundamental mode, as shown by Fig. 4. Fig. 5B-C show the distribution of the parameters linked to the best simulations: wet layer thickness and wet layer velocity, respectively.

We averaged the parameters of the best simulations to achieve an estimated value for both the velocity and the thickness of the wet layer, at all times. Statistics and ranges of the considered best simulations are summarized in Table 3. The velocity of the wet layer changes slightly over time, with values confined in a narrow range, in all cases very far from the value of the dry sand (0.14 m/ns).

We are less confident in the inversion of time t_2 for two reasons: (1) the fitting between measured and calculated data is poor respect to the other time-steps that show high values of NSI; (2) the experimental dispersion curve is derived from the *f-k* domain, that shows that energy is smeared between fundamental and first higher mode. Therefore, the dispersion curve at time t_2 may be heavily affected by the unfavorable signal to noise ratio for both the fundamental and the first higher mode.

It should also be noted that our MC inversion provides a view of the degree of correlation of the two governing parameters (thickness and velocity of the wet layer). Fig. 6 shows the levels of NSI>0.85 plotted in the parameter space, highlighting some degree of positive correlation. However, at times t_1 and t_3 the best fitting simulations (NSI>0.984 for t_1, NSI>0.987 for t_3), marked as a green area, are centered around small parameter ranges. At time t_2 the green area highlights the simulations with NSI>0.886. Table 3 reports the standard deviations of the parameters associated to the best-fitting simulations that are quite small with respect to the average values.

5. ERT DATA ANALYSIS

The ERT data were collected at the surface using a Syscal-Pro resistivimeter (IRIS Instruments, France). Twenty-four electrodes spaced 20 cm were placed on a transect perpendicular to the sprinklers' line, for a total length of 4.6 m (Fig. 1). The acquisition scheme was a dipole-dipole skip zero (dipoles with minimal distance equal to one electrode spacing). Reciprocal measurements were acquired and processed to estimate data errors. All the reciprocal measures with the statistical operator RSD (Relative Standard Deviation) exceeding the 5% were removed from the dataset. This reciprocal error analysis leads to a different dataset for each time step. For this reason and to have comparable results, we performed the inversions considering only the quadripoles that are present in all datasets. The common datasets preserve 200 measurements over a total of 231 quadripoles, thus data quality is particularly good. We inverted the data as the ratio of electrical resistances at a specific time with respect to the resistance values at the background measurement (in our case the time-step before the irrigation):

$$R = \frac{R_i}{R_0} \cdot R_{hom} \qquad (8)$$

Where R_i is the electrical resistance at the *i*-th time-step, R_0 is the electrical resistance at the background measure and R_{hom} is the electrical resistance for a homogenous space of 100 Ωm. All the electrical resistances are referred to the same quadripole and R is calculated for each measurement in the dataset. As data errors are difficult to estimate in terms of resistance ratios, some degree of arbitrary choice is present in ratio inversion. Fig. 7A shows the inversion of the resistivity ratios with respect to background (Eq. 8) applying a smoothness constrain of 3%.

This time-lapse ratio inversion clearly shows the variation of the electrical resistivity during the experiment (Fig. 7A). The results of the inversion are sections of the percentage variation of resistivity respect to the background values: values equal to 100 Ωm correspond to unchanged resistivity, while values less or more than 100 Ωm show a decreasing or an increasing resistivity, respectively. The inversions were performed using the 2D code developed by Andrew Binley (http://www.es.lancs.ac.uk/people/amb/Freeware/Freeware.htm; Slater et al. 2000; Cassiani and Binley, 2005; Linde et al., 2006).

Fig. 7B shows the results of the ratio of the inverted absolute profiles with respect to the inversion of the background survey. In this case the profiles are inverted with a data error set at 5%, consistent with the reciprocal error removal procedure, and then a pixel by pixel ratio is computed. From the comparison between Fig. 7A and 7B it is apparent that the two approaches are, in this case, essentially equivalent at showing the evolution of the infiltration process. This similarity corroborates the hypothesis of the 2D symmetry of the infiltration process along the sprinkler line, since the ERT monitoring is performed on 2D profiles, assuming a homogeneous resistivity distribution on the third direction.

In Fig. 7 the infiltration process is clearly visible. The plume of injected fresh water increases moisture content and consequently reduces resistivity. The shape of the plume is the consequence of a non-uniform distribution of irrigation in the direction perpendicular to the sprinklers' line. The distribution of the artificial precipitation is more likely Gaussian in shape, with considerably more water dropping close to the sprinklers. Time-steps t_5 and t_7 are not shown, as only modest variations are present at these late times after the end of the irrigation.

6. SETUP OF THE COUPLED INVERSION

In this work the modeling based on the coupled-inversion described in Section 2 is aimed specifically at the estimation of soil saturated hydraulic conductivity. The physically-based hydrological model CATHY (Camporese et al., 2010) is employed for the numerical solution of Eq. (1) and the simulation of the infiltration experiment. The van Genuchten's parameters necessary for the setup of the numerical model were derived from laboratory experiments: residual saturation is fixed at 0.003 and α (the inverse of the air entry suction) is equal to 5.4 m^{-1}. These values are derived from laboratory experiments and are not considered of paramount importance in the context of the given infiltration experiment. Of course a more complete parameter identification scheme could also include them, as described by Manoli et al. (2015) in the context of using ERT data alone.

A careful analysis of Fig. 7 reveal that irrigation was not uniformly distributed in the direction orthogonal to the sprinkler line, probably due to the presence of wind. This was taken into account in order to properly simulate the top boundary conditions: the irrigation is modeled with a Gaussian distribution centered at 2.5 m, with variance equal to 0.6 m, both values calculated such that the total flux equals the real irrigation rate. The parameters of the Gaussian distribution are fixed after a trial procedure where we matched the shape of the measured and modeled plume (Fig. 7 and Fig. 10).

The parameters of Archie's law (Eq. 3), which are necessary to define the ERT observation operator, are spatially uniform for considered field study. The exponent n is set to 1.27 as reported in Cassiani et al. (2009c), where the value is obtained from laboratory calibration on the site's sediments. The initial soil electrical resistivity $\rho(t_0)$ is set equal to 1300 Ωm, based on the averaged value obtained by the inversion of background ERT measures. In order to apply Eq. (3), we need also an estimation of the initial volumetric water content, $\theta(t_0)$. For our field experiment this is estimated from background GPR and TDR measurements. A value $\theta(t_0) = 0.07$ is obtained by applying the petrophysical relationship of Topp et al. (1980):

$$\theta = (-530 + 292\varepsilon_r - 5.5{\varepsilon_r}^2 + 0.043{\varepsilon_r}^3) \cdot 10^{-4} \tag{5}$$

where ε_r is the bulk soil dielectric permittivity. A moisture content value of 7% corresponds to $S_w(t_0)$ of 0.212 assuming a porosity of 0.33 as estimated by Cassiani et al. (2009b) for the considered field sediments.

In this particular case, we are interested in the value of the saturated hydraulic conductivity $\boldsymbol{K_s}$, that is difficult to identify in unsaturated conditions by direct measurements. The methodology presented in Manoli et al. (2015) describes $\boldsymbol{K_s}$ with a lognormal probability distribution which mean and variance are updated at each assimilation time. Here, the prior values of the hydraulic conductivity mean and variance are summarized in Table 5.

The iterative procedure is particularly advantageous when geophysical measurements of different nature (e.g. ERT and GPR) are available for the assimilation, as in the case we consider here. In fact, the independent assimilation of different measurements is to prefer to the joint assimilation of the measurements, since the latter requires the introduction of an artificial normalization to weight the measurements.

In this paper the procedure is used to provide the "best possible" estimate of $\boldsymbol{K_s}$ for the site using both ERT and GPR data. We adopt a strategy that is particularly clear in assessing the information content of each dataset and of the two datasets together. In particular, we produce the following four assimilation schemes:

A. a scheme assimilating only ERT data (similar to the one proposed by Manoli et al., 2015);

B. a scheme assimilating only GPR data, based on the depth of the infiltration front estimated from the guided wave analysis (see section 3);

C. a scheme that assimilates alternatively ERT and GPR leading to a final estimate that accounts for both;

D. a scheme analogous to C, but using GPR and ERT in the reverse order – to check convergence stability (the first iteration starts assimilating GPR data, instead of ERT data).

The advantage of assimilating both ERT and GPR measurements is the integration of different information. In this kind of experiment (irrigation monitored on the ground surface), the low sensibility of the ERT array at large depths may be a disadvantage; so the infiltration front may be spread over a broad area, since the most part of the energy is focalized along current paths that cross the wet zone. GPR WARR surveys may be a useful addition to the information obtained from ERT, as GPR can constrain the location of the water front at depth.

7. MODELLING RESULTS

The particle filter algorithm assimilates the geophysical data with four different schemes (Fig. 8). Each assimilation scheme leads to a probability distribution of the simulated parameters: in this case $\boldsymbol{K_s}$ is the objective of the coupled inversion. The evolution of the $\boldsymbol{K_s}$ distribution during the assimilation procedures is summarized in Fig. 8. For each assimilation scheme, 3 different prior $\boldsymbol{K_s}$-distributions are tested to verify the stability of the inversion procedure. It evinces that the convergence towards the estimated $\boldsymbol{K_s}$ value, at the end of the iteration process, is not depending on the initial parameter's range.

The estimated values of $\boldsymbol{K_s}$ are only slightly different from scheme to scheme: for case *A*: 1.010^{-5} m s^{-1}, for case *B*: 2.6 10^{-5} m s^{-1}, for case *C*: 1.1 10^{-5} m s^{-1}, for case *D*: 1.1 10^{-5} m s^{-1}. Note that the differences in the estimated $\boldsymbol{K_s}$ are almost negligible for practical applications. Assimilating both ERT and GPR we obtain the same $\boldsymbol{K_s}$value, irrespective of the order of assimilation. The assimilation of only ERT data (Fig. 8A) provides a $\boldsymbol{K_s}$ estimate that is very similar to the ERT-GPR assimilations. The assimilation of the GPR waterfront depths provides a value of $\boldsymbol{K_s}$ about two times larger than the other estimates (Fig. 8B). We attribute this results to the large uncertainty associated to the GPR measurement and analysis, in particular at the time *t2*.

Forward hydrological models are then run with the estimated parameters and the results are compared to the geophysical measurements (Tables 4 and 6). Schemes C and D provide essentially the same hydrological model. The mean and standard deviations of the posterior distributions for the four cases are listed in Table 5 (together with the prior parameters).

In Table 4 the waterfront position inverted from the GPR signal is compared to the simulated location of the saturation front. Note that the water front locations estimated from the coupled inversions with the GPR assimilation leads to slightly deeper water front estimations, while ERT and ERT-GPR assimilations conduct to very similar results. The GPR contribution in the combined inversion with ERT drives the estimated waterfront slightly deeper than estimated by ERT only. The waterfront depths from GPR data alone are definitely more problematic to interpret (see also Fig. 9), with uneven penetration speed between time intervals 1-2 and 2-3. Note that, as discussed in Section 3, time 2 is a problematic acquisition for GPR, with energy spread over two modes and a more difficult estimation of infiltration front depth.

The forward hydrological models are also compared against the ERT field (resistance) dataset (Tab. 5). In this case the simulated hydrological states are converted into geophysical quantities via Eq. 4, and a geophysical forward model (Eq. 3) is run to obtain simulated ERT resistance data. Not surprisingly, the forward model that best matches the field measurements is derived from the assimilation of the sole ERT data. Anyway the assimilation of both ERT and GPR shows a very good fit to the measured ERT, while the assimilation scheme of only GPR-derived waterfronts is distant from the information achieved from ERT survey.

Fig. 9 shows the distribution of moisture content predicted by the flow models with the parameters obtained from data assimilation. These saturation profiles are compared against:

1. the moisture content profiles one could obtain by translating directly the resistivity inverted images (Fig. 7) using the known Archie's law parameters (Eq. 4).
2. the locations of the infiltration front as estimated from GPR inversion (Section 3).
3. the estimation of the degree of saturation measured by TDR probes placed at the mid-point of the ERT profile; relative dielectric permittivity is translated into water content using Eq. (5).

There is no doubt that the data assimilated simulations are superior at providing estimates of moisture content profiles that, while slightly different from each other, are both consistent with data and model assumptions (most of all, mass balance and hydraulic conductivity homogeneity).

The TDR data are used as validation of the modeled water saturation curves (Fig. 9). The values are consistent with the hydrological models, that show a rapidly-moving saturation front at the first time steps. Unfortunately the TDR probes reach the maximum depth of only 0.3 m, so no information is available for the deeper portions.

For the sake of completeness, we also inverted the synthetic ERT data (Fig. 7C) to provide a direct comparison with the ρ distributions achieved by field measurements (Fig. 7A). In addition, Fig. 10 shows the “true” resistivity structure as simulated by the hydrological model in the combined ERT-GPR data assimilation case. Comparing Figs. 7 and 10, note how inverted and “true” resistivity images tend to diverge at late times, when the front reaches the deeper zones where ERT has the lowest sensitivity, and inversion regularization takes over and smears the images at depth. Consistently, the mass balance derived from ERT data as calculated for the coupled and the uncoupled hydro-geophysical inversions (Table 7) shows the weaknesses of the uncoupled approach for the problem at hand. The uncoupled approach leads to a cumulative volume of injected water over time that strongly overestimates the effective amount of irrigated water.

Note that in the literature underestimation of mass balance is more commonly observed (e.g., Singha and Gorelick, 2005), but this fact is dependent primarily on the acquisition scheme and electrode geometrical configuration (e.g. cross-hole versus surface measurements, as in this work).

8. CONCLUSIONS

Hydro-geophysical techniques are extremely useful in monitoring the hydrological processes acting in the vadose zone and the data can be effectively translated into hydrological quantities, particularly state variables such as moisture content. The presented field case study analyzes a controlled irrigation test in an unsaturated subsoil with a plain terrain and nearly homogeneous sandy soil.

The adopted hydro-geophysical methodology may strongly affect the results of the hydro-geophysical inversion and consequently the hydrological parameter estimations. An approach, that fully couples hydrological modeling and geophysical measurements in a data assimilation procedure, leads to more accurate results. Avoiding the geophysical inversion of the data, we reduce the uncertainty in the hydrological quantities estimation, since no artifacts are inserted in the method by solving an inverse problem. The errors that may be present are due only to data acquisition and model choosing, as in any hydro-geophysical issue. Of course an analysis of the inverted data is generally necessary, not only to ascertain the data quality, but also to direct a correct choice of the hydrological model needed to explain the data (see, e.g., discussion in Camporese et al., 2011). One of the advantages of the coupled approach, that includes a stochastic process, is the proper conservation of mass. This aspect is often a key issue of the uncoupled approach, where the calibration of hydrological models via geophysical inverted data may lead to inconsistent results that may jeopardize the user's confidence in the method.

In the present field case both ERT and the infiltration front estimated with the GPR data are considered in the data assimilation process, using a Sequential Importance Resampling (SIR) that allows a flexible assimilation of either or both datasets in a natural, non-subjective manner (i.e. without arbitrary weighting of one dataset with respect to the other). From this procedure the information content of each dataset in the assimilation procedure emerges naturally.

In this particular case study, it is apparent that ERT data provide most of the information needed to a robust hydraulic conductivity estimation. GPR, albeit being apparently of easy interpretation in its time-lapse evolution (see Figure 3), at a more in-depth quantitative analysis shows its intricacies linked to the inversion of multi-modal dispersion guided waves. As the energy distribution over different modes changes over time due to the changing geometry of the wet layer, the inversion of GPR data requires particular attention and ultimately delivers weak information on the infiltration process.

The comparison between coupled and uncoupled hydro-geophysical inversions shows that, in this particular case, the latter is superior. This happens primarily because the monitoring of type of experiment that we consider (irrigation and infiltration from the ground surface) depends strongly on our ability to image the processes honoring mass balance. In this respect, the uncoupled approach is not capable of reproducing the real state of the system and consequently the mass balance. The uncoupled approach may therefore lead to erroneous parameter estimate. It should be noted how other problems may be less prone to suffering from an uncoupled approach (see e.g. Camporese et al., 2011).

ACKNOWLEDGEMENTS

The authors would like to acknowledge support from the EU FP7 Collaborative Projects CLIMB ("Climate Induced Changes on the Hydrology of Mediterranean Basins - Reducing Uncertainty and Quantifying Risk"). This study was also funded by the University of Padova, Italy, within the Research Programme "GEO-RISKS: Geological, morphological and hydrological processes: monitoring, modeling and impact in the north-eastern Italy". Partial funding was also provided by the EU FP7 project GLOBAQUA ("Managing the effects of multiple stressors on aquatic ecosystems under water scarcity").

REFERENCES

Archie GE. The electrical resistivity log as an aid in determining some reservoir characteristics. *Trans. AIME* 1942; 146: 54–62.

Arcone SA, Peapples PR, and Liu L. Propagation of a ground-penetrating radar (GPR) pulse in a thin waveguide. *Geophysics* 2003; 68(6): 1922-1933.

<u>ASTM D2487 - Standard Practice for Classification of Soils for Engineering Purposes (Unified Soil Classification System).</u>

Becht A, Appel E, and Dietrich P. Analysis of multi-offset GPR data: a case study in a coarse-grained gravel aquifer. *Near Surf. Geophys.* 2006; 4(4): 227-240.

Binley A, Henry-Poulter S, and Shaw B. Examination of solute transport in an undisturbed soil column using electrical resistance tomography. *Water Resour. Res.* 1996; 32: 763-769.

Binley AM and Kemna A. DC resistivity and induced polarization methods. In: Rubin Y, Hubbard SS, editors. *Hydrogeophysics. Water Sci. Technol. Library*, Ser. 50, Springer, New York; 2005, p. 129-156.

Bohidar RN and Hermance JF. The GPR refraction method. *Geophysics* 2002; 67(5): 1474-1485.

Brovelli A and Cassiani G. Effective permittivity of porous media: a critical analysis of the complex refractive index model. *Geophys. Prospect.* 2008; 56(5): 715–727, doi: 10.1111/j. 1365-2478.2008.00724.x

Brovelli A and Cassiani G. Combined estimation of effective electrical conductivity and permittivity for soil monitoring. *Water. Resour. Res.* 2011; 47(8): W08510, doi:10.1029/2011WR010487

Busch S, van der Kruk J, Bikowski J, and Vereecken H Quantitative conductivity and permittivity estimation using full-waveform inversion of on-ground GPR data. *Geophysics* 2012; 77(6): H79-H91, doi: 10.1190/GEO2012-0045.1

Busch S, Weihermuller L, Huisman JA, Steelman CM, Endres LA, Vereecken H, and van der Kruk J. Coupled hydrogeophysical inversion of time-lapse surface GPR data to estimate hydraulic properties of a layered subsurface. *Water. Resour. Res.* 2014; 49(12): 8480-8494, doi:10.1002/2013WR013992

Camporese M, Paniconi C, Putti M, and Orlandini S. Surface-subsurface flow modeling with path-based runoff routing, boundary condition-based coupling, and assimilation of multisource observation data. *Water Resour. Res.* 2010; 46(2): W02512, doi:10.1029/2008WR007536Camporese M., G. Cassiani, R. Deiana and P. Salandin, 2011, Assessment of local hydraulic properties from electrical resistivity tomography monitoring of a three-dimensional synthetic tracer test experiment, *Water Resources Research*, 47, W12508, doi:10.1029/2011WR010528, 2011.

Caputo MC, De Carlo L, and Masciale R. Hydrogeophysical approach to measure hydraulic parameters on unsaturated rocks. *Fresen. Environ. Bulletin* 2012; 21(10A): 3077-3082.

Cassiani G and Binley A Modeling unsaturated flow in a layered formation under quasi-steady state conditions using geophysical data constraints. Adv. Water Resour. 2005; 28(5): 467-477.

Cassiani G, Binley AM, and Ferré TPA. Unsaturated zone processes. In: Vereecken H et al. editors. *Applied Hydrogeophysics*, Springer-Verlag, Berlin; 2006; 71: p. 75-116.

Cassiani G, Fusi N, Susanni D, and Deiana R. Vertical radar profiling for the assessment of landfill capping effectiveness. *Near Surf. Geophys*. 2008; 6(2): 133-142, doi: 10.3997/1873-0604.2008010

Cassiani G, Godio A, Stocco S, Villa A, Deiana R, Frattini P, and Rossi M. Monitoring the hydrologic behaviour of a mountain slope via time-lapse electrical resistivity tomography. *Near Surf. Geophys.* 2009a; 7(5-6): 475-486.

Cassiani G, Giustiniani M, Ferraris S, Deiana R, and Strobbia C, Time-lapse surface-to-surface GPR measurements to monitor a controlled infiltration experiment. *B. Geofis. Teor. Appl.* 2009b; 50(2): 209-226.

Cassiani G, Kemna A, Villa A, and Zimmermann E. 2009c. Spectral induced polarization for the characterization of free-phase hydrocarbon contamination of sediments with low clay content. *Near Surf. Geophys.* 2009c; 7(5-6): 547–562, doi:10.3997/1873-0604.2009028

Cassiani G, Ursino N, Deiana R, Vignoli G, Boaga J, Rossi M, Perri MT, Blaschek M, Duttmann R, Meyer S, Ludwig R, Soddu A, Dietrich P, and Werban U. Non-invasive monitoring of soil static characteristics and dynamic states: a case study highlighting vegetation effects. *Vadose Zone J*. 2012; 11(3), doi: 10.2136/2011.0195

Clément R, Descloitres M, Günther T, Ribolzi O, and Legchenko A. Influence of shallow infiltration on time-lapse ERT: Experience of advanced interpretation. *C. R. Geosci*. 2009; 341(10-11): 886-898, doi: 10.1016/j.crte.2009.07.00

Daily W, Ramirez A, LaBrecque D, and Nitao J. 1 Electrical resistivity tomography of vadose water movement. *Water Resour. Res.* 1992; 28(5): 1429-1442.

Day-Lewis FD, Singha K, and Binley AM. Applying petrophysical models to radar travel time and electrical resistivity tomograms: Resolution-dependent limitations. *J. Geophys Res.-Sol. Ea*. 2005; 110(B8): B08206.

Ferré TPA, Bentley L, Binley A, Linde N, Kemna A, Singha K, Holliger K, Huisman S, and Minsley B. Critical steps for the continuing advancement of hydrogeophysics. *EOS T. Am. Geophys. Un*. 2009; 90(23): 200.

Fisher E, McMechan GA, and Annan AP. Acquisition and processing of wide-aperture ground-penetrating radar data. *Geophysics* 1992; 57(3): 495–504.

Gelagedara LW, Parkin GW, Redman JD, von Bertoldi P, and Endres AL. Field studies of the GPR ground wave method for estimating soil water content during irrigation and drainage. *J. Hydrol.* 2005; 301(1-4): 182-197, doi: 10.1016/j.jhydrol.2004.06.031

Gerlitz K, Knoll MD, Cross GM, Luzitano RD, and Knight R. Processing ground penetrating radar data to improve resolution of the near-surface targets. In: *Proceedings of the Symposium on the Application of Geophysics to Engineering and Environmental Problems*; 1993: 561-575

Greaves RJ, Lesmes DP, Lee JM, and Toksoz MN. Velocity variations and water content estimated from multi-offset ground-penetrating radar. *Geophysics* 1996; 61(3): 683-695, doi: 10.1190/1.1443996

Hinnell AC, Ferré TPA, Vrugt JA, Huisman JA, Moysey S, Rings J, and Kowalsky MB. Improved extraction of hydrologic information from geophysical data through coupled hydrogeophysical inversion. *Water Resour. Res.* 2010; 46(4): W00D40, doi: 10.1029/2008WR007060

Hubbard SS, Grote K, and Rubin Y. Mapping the volumetric soil water content of a California vineyard using high-frequency GPR ground wave data. *The Leading Edge* 2002; 21: 552–559.

Huisman JA, Sperl C, Bouten W, and Verstraten JM. Soil water content measurements at different scales: accuracy of time domain reflectometry and ground-penetrating radar. *J. Hydrol*. 2001; 245(1-4), 48–58.

Huisman JA, Hubbard SS, Redman JD, and Annan AP. Measuring soil water content with ground penetrating radar: a review. *Vadose Zone J.* 2003; 2(4): 477-491.

Klotzsche A, van der Kruk J, Meles G, and Vereecken H. Crosshole GPR full-waveform inversion of waveguides acting as preferential flow paths within aquifer systems. *Geophysics* 2012; 77(4): H57-H62.

Klotzsche A, van der Kruk J, Linde N, Doetsch J, and Vereecken H. 3-D characterization of high-permeability zones in a gravel aquifer using 2-D crosshole GPR full-waveform inversion and waveguide detection. *Geophys. J. Int.* 2013; 195(2): 932-944.

La Brecque DJ, Heath G, Sharpe R, and Versteeg R. Autonomous monitoring of fluid movement using 3-D electrical resistivity tomography. *J. Environ. Eng. Geoph.* 2004; 9(3): 167-176.

Lai W.L., S.C. Kou and C.S. Poon, 2012 Unsaturated zone characterization in soil through transient wetting and drying using GPR joint time-frequency analysis and grayscale images. *J. Hydrol.* 2012; 452-453: 1-13, doi: 10.1016/j.jhydrol.2012.03.044

Lambot S, Slob EC, van den Bosch I, Stockbroeckx B, and Vanclooster M. Modeling of ground-penetrating radar for accurate characterization of subsurface electric properties. *IEEE T. Geosci. Remote*, 2004; 42(11): 2555-2568.

Linde N, Binley A, Tryggvason A, Pedersen L, and Revil A. Improved hydrogeophysical characterization using joint inversion of cross-hole electrical resistance and ground-penetrating radar traveltime data. *Water Resour. Res.* 2006; 42(12): W04410, doi:10.1029/2004WR003806

Manoli G., M. Rossi, D. Pasetto, R. Deiana, S. Ferraris, G. Cassiani and M. Putti, 2015, An iterative particle filter approach for coupled hydro-geophysical modeling and inversion of a controlled infiltration experiment, *Journal of Computational Physics*, pp 37-51, doi: 10.1016/j.jcp.2014.11.035Mangel AR, Moysey SMJ, Ryan JC, and Tarbutton JA. Multi-offset ground-penetrating radar imaging of a lab-scale infiltration test. *Hydrol. Earth Syst. Sc*. 2012; 16: 4009-4022, doi: 10.5194/hess-16-4009-2012.

McLaughlin D. An integrated approach to hydrologic data assimilation: interpolation, smoothing, and filtering. *Water Res. Resour*. 2002; 25(8-12): 1275-1286.

Menke W. *Geophysical Data Analysis: Discrete Inverse Theory*. Elsevier, New York; 1984.

Michot D, Benderitter Y, Dorigny A, Nicoullaud B, King D, and Tabbagh A. Spatial and temporal monitoring of soil water content with an irrigated corn crop cover using surface electrical resistivity tomography. *Water Res. Resear.*, 2003; 39(5): 1138. doi:10.1029/2002WR001581.

Moradkhani H, Hsu K-L, Gupta H, and Sorooshian S. Uncertain assessment of hydrologic model states and parameters: Sequential data assimilation using the particle filter. *Water Res. Resear.* 2005; 41(5), doi: 10.1029/2004WR003604

Moysey SMJ. Hydrologic trajectories in transient ground-penetrating radar reflection data. *Geophysics*, 2010; 75(4): WA211-WA219, doi: 10.1190/1-3463416

Nash JE and Sutcliffe JV. River flow forecasting through conceptual models part I — A discussion of principles. *J. Hydrol.* 1970; 10(3): 282–290.

Perri MT, Cassiani G, Gervasio I, Deiana R, Binley AM. A saline tracer test monitored via both surface and cross-borehole electrical resistivity tomography: Comparison of time-lapse result., *J. App. Geophys.* 2012; 79: 6-16, doi:10.1016/j.jappgeo.2011.12.011

Rings J, Huisman JA, and Vereecken H, 2010. Coupled hydrogeophysical parameter estimation using a sequential Bayesian approach. *Hydrol. Earth Syst. Sc.* 2010; 14: 545-556.

Rossi M, Cassiani G, and Binley A. A stochastic analysis of cross-hole gpr zero-offset profiles for subsurface characterization. *Vadose Zone J.* 2012; 11(4), doi: 10.2136/vzj2011.0078

Roth K, Schulin R, Fluhler H, and Hattinger W. Calibration of time domain reflectometry for water content measurements using a composite dielectric approach. *Water Resour. Res.* 1990; 26(10): 2267-2273.

Rucker DF and Ferré TPA. Correcting water content measurement errors associated with critically refracted first arrivals on zero offset profiling borehole ground penetrating radar profiles. *Vadose Zone J*. 2004a; 3(1): 278-287.

Rucker DF and Ferré TPA. Parameter estimation for soil hydraulic properties using zero-offset borehole radar. *Soil Sci. Soc. Am. J.* 2004b; 68(5): 1560-1567.

Schmelzbach C, Tronicke J, and Dietrich P. High-resolution water content estimation from surface-based ground-penetrating radar reflection data by impedance inversion. *Water Resour. Res.* 2012; 48(8): W08505, doi:10.1029/2012WR011955

Singha K and Gorelick SM. Saline tracer visualized with three-dimensional electrical resistivity tomography: Field-scale spatial moment analysis. *Water Resour. Resear.* 2005; 41(5), W05023, doi:10.1029/2004WR003460

Slater L, Binley AM, Daily W, and Johnson R. Cross-hole electrical imaging of a controlled saline tracer injection. *J. App. Geophys.* 2000; 44(2-3): 85-102.

Steelman CM, Endres AL, and Jones JP., 2012,High-resolution ground-penetrating radar monitoring of soil moisture dynamics: Field results, interpretation, and comparison with unsaturated flow model. *Water Resour. Res.* 2012; 48(9): W09538, doi: 10.1029/2011WR011414

Strobbia C and Cassiani G. Multi-layer GPR guided waves in shallow soil layers for the estimation of soil water content. *Geophysics* 2007; 72(4): J17–J29, doi: 10.1190/1.2716374

Topp GC, Davis JL, and Annan AP. Electromagnetic determination of soil water content: measurements in coaxial transmission lines. *Water Resour. Res.* 1980; 16(3): 574–582.

Tran A.P,, M. Vanclooster, M.Zupanski, and S. Lambot, 2014, Joint estimation of soil moisture profile and hydraulic parameters by ground-penetrating radar data assimilation with maximum likelihood ensemble filter. *Water Resour. Res.* 2014; 50(4): 3131–3146, doi: 10.1002/2013WR014583

Travelletti J, Sailhac P, Malet J-P, Grandjean G, and Ponton J., 2012,Hydrological response of weathered clay-shale slopes: water infiltration monitoring with time-lapse electrical resistivity tomography. *Hydrol. Process.* 2012;, 26(14): 2106-2119, doi: 10.1002/hyp.7983

van der Kruk J, Streich R, and Green AG. Properties of surface waveguides derived from separate and joint inversion of dispersive TE and TM GPR data. *Geophysics* 2006; 71(1): K19-K29.

van Genuchten MT and Nielsen DR. On describing and predicting the hydraulic properties of unsaturated soils. *Ann. Geophys*. 1985; 3(5): 615–628.

van Overmeeren RA, ,Sariowan SV, and Gehrels JC. Ground penetrating radar for determining volumetric soil water content: Results of comparative measurements at two test sites. *J. Hydrol.* 1997;,197(1-4): 316–338.

Vignoli G, Deiana R, and Cassiani G, Focused inversion of vertical radar profile (VRP) traveltime data. *Geophysics* 2012; 77(1): H9-H18, doi: 10.1190/GEO2011-0147.1

978 # TABLES

Irrigation steps	Irrigation start [min]	Irrigation end [min]	Cumulative water volume [m^3]
1	0	115	2.509
2	146	233	4.127
3	264	327	5.652

Table 1. *Time schedule and irrigated volumes for the infiltration experiment.*

Geophysical techniques	Starting time of the survey [min]								
	Background t_0	t_1	t_2	t_3	t_4	t_5	t_6	t_7	t_8
GPRWARR	-10	115	233	327	-	-	-	-	-
ERT	-5	120	240	335	1030	1150	1420	1480	1540

Table 2. *Time schedule of the geophysical acquisitions; time is referred to the irrigation start.*

Time step	Averaged thickness [m]	Standard deviation of thickness [m]	Averaged velocity [m/ns]	Standard deviation of velocity [m/ns]	Number of averaged simulations	NSI range of averaged simulations
t_1	0.46	0.031	0.091	0.0013	197	0.984-0.987
t_2	0.49	0.019	0.074	0.0006	106	0.886-0.889
t_3	0.74	0.016	0.081	0.0007	83	0.987-0.990

Table 3. *Statistics of the GPR slab waveguide simulations that best fit the measured dispersion curves.*

Time-step	t_1 (m)	t_2 (m)	t_3 (m)	*Mean Error* (m)
GPR inversion	-0.46	-0.49	-0.74	
Posterior ERT	-0.32	-0.52	-0.66	0.083
Posterior GPR	-0.38	-0.61	-0.79	0.083
Posterior ERT-GPR	-0.34	-0.54	-0.70	0.070

Table 4. *Infiltration front depth for the first three time-steps, obtained from GPR-EM-waveguide inversion and from posterior hydrological forward models. The last column is the average absolute error between the waterfront positions measured with the GPR and those estimated with the posterior hydrological forward models.*

Prior distribution		**Posterior distribution**							
		ERT		GPR		ERT+GPR		GPR+ERT	
Mean	St. dev.	Mean	St. dev.	Mean	St. dev.	Mean	St. dev.	Mean	St. dev.
m/s	m/s	10^{-5} m/s	10^{-5} m/s	10^{-5} m/s	10^{-5} m/s	10^{-5} m/s	10^{-5} m/s	10^{-5} m/s	10^{-5} m/s
1×10^{-7}	1×10^{-7}	0.99	0.014	2.50	0.148	1.15	0.014	1.11	0.015
1×10^{-5}	1×10^{-5}	1.02	0.008	2.63	0.083	1.14	0.076	1.08	0.018
1×10^{-3}	1×10^{-3}	0.90	0.018	2.86	0.053	1.17	0.032	1.06	0.012

Table 5: Prior and posterior distributions of the hydraulic conductivity $\mathbf{K}_S$ for the different data assimilation schemes

Time-step	t_1	t_2	t_3	t_4	t_5	t_6	t_7	t_8	*Mean*
Posterior ERT	3.5	4.3	3.7	3.1	3.1	3.4	3.5	3.6	3.525
Posterior GPR	3.6	4.4	3.7	4.4	4.5	5.1	5.3	5.4	4.550
Posterior ERT-GPR	3.5	4.2	3.6	3.2	3.2	3.6	3.7	3.8	3.600

Table 6.*Root mean square relative error between the field measured electric resistance value sand those simulated with the posterior hydrological forward models (results in %). The last column is the mean in time of these errors. The relative error is adopted because the electric resistances vary over several orders of magnitude.*

Irrigation steps	Irrigation time [min]	Cumulative water volume				
		Effective injected volume[m³]	Coupled model		Uncoupled model	
			Volume [m³]	% error	Volume [m³]	% error
1	115	2.509	2.354	6.2	4.181	66.6
2	233	4.127	3.997	3.1	7.713	86.9
3	327	5.652	5.564	1.6	9.559	69.1

Table 7. *Mass balance achieved with coupled and uncoupled hydro-geophysical inversions.*

FIGURES

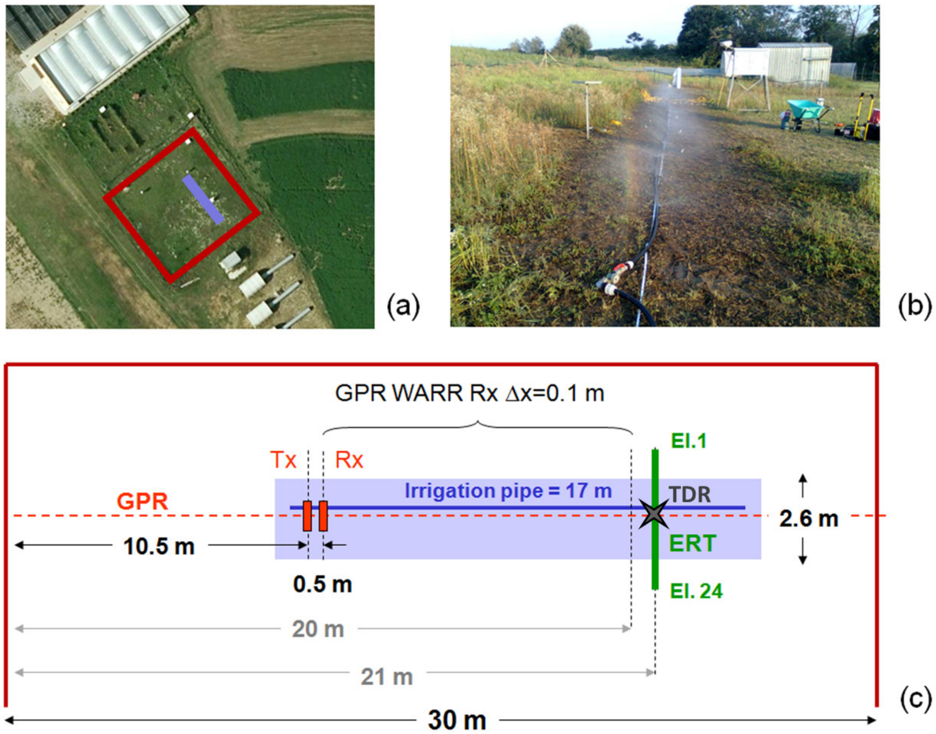

Figure 1. *Scheme and location of the experiment: (a) aerial view of the field with the irrigated zone highlighted in blue; (b) the sprinkler line during the irrigation; (c) scheme of the geophysical surveys and position of the irrigated soil.*

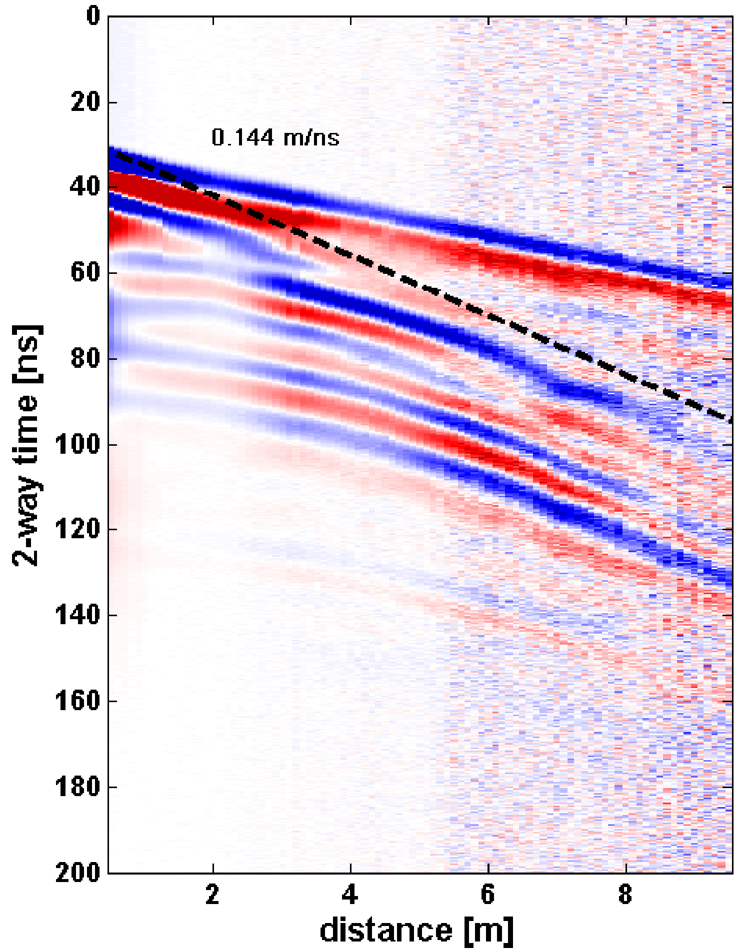

Figure 2. *Background WARR survey with the identification of the direct wave through the ground.*

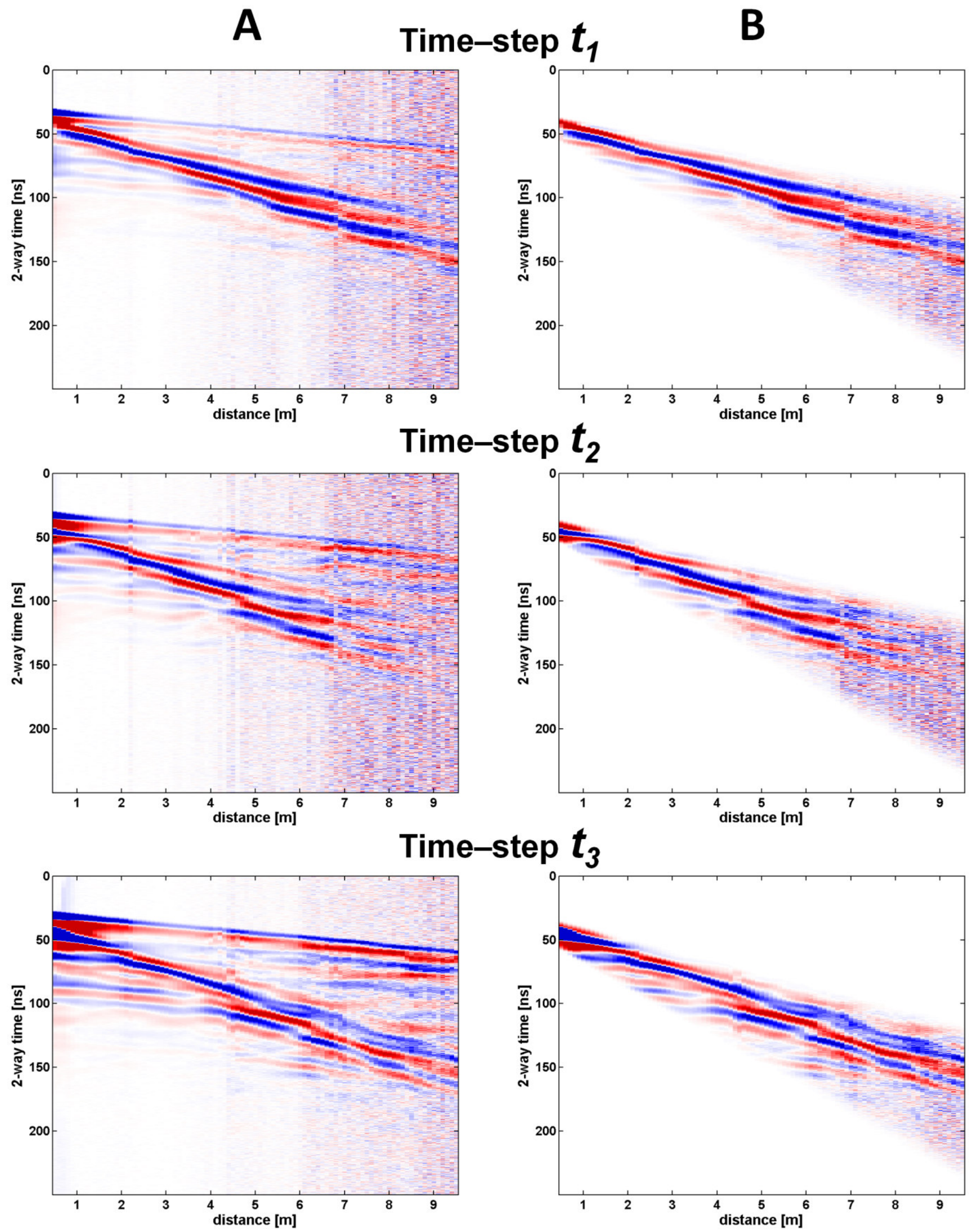

Figure 3. *Field measured WARR radargrams at the times t_1, t_2 and t_3. A) On the left, the radargrams are filtered only by the "dewow" procedure (traces are normalized). B) On the right, the same radargrams are displayed after the preprocessing (muting and FIR filter).*

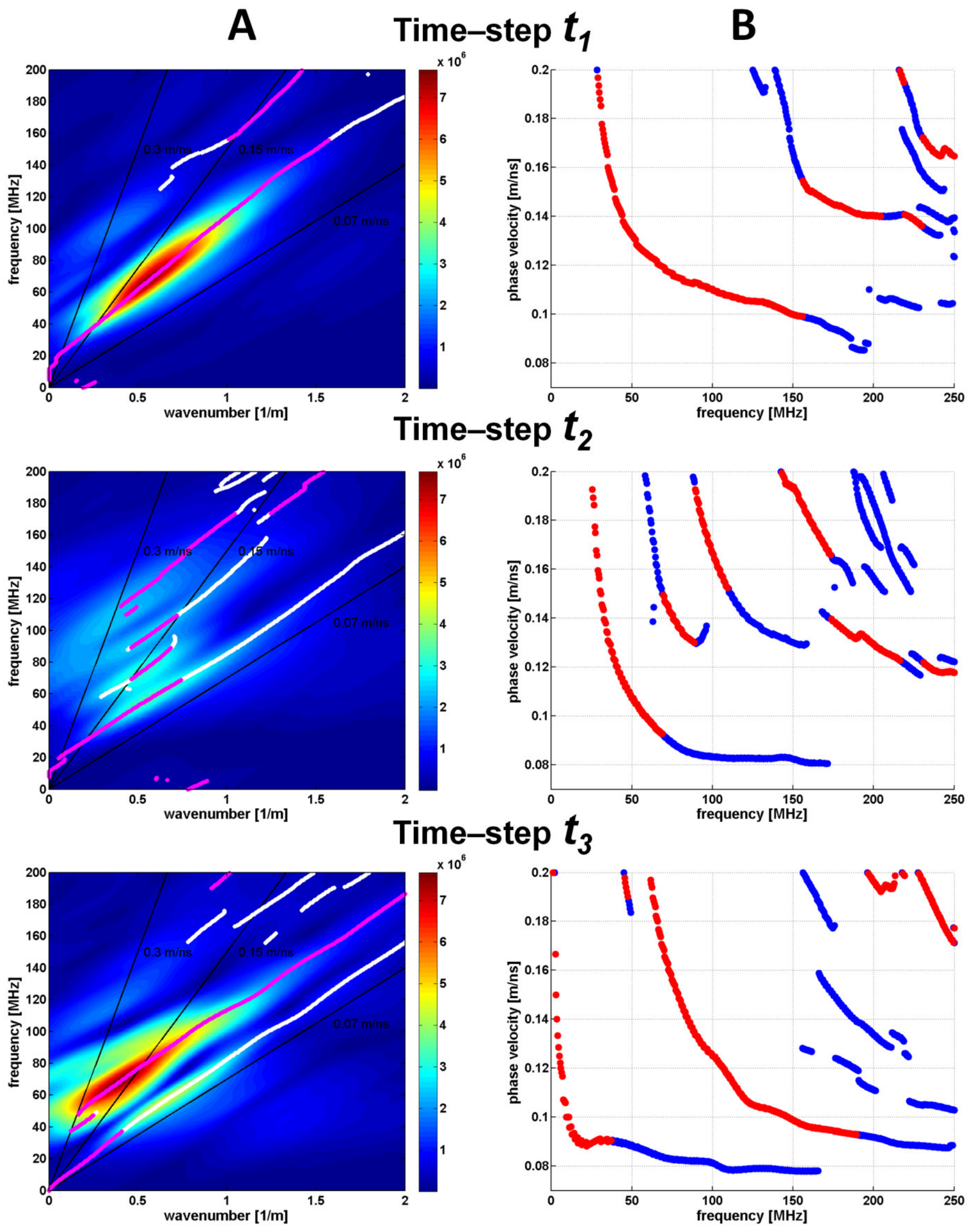

Figure 4. *Analysis of the GPR soundings in the frequency domain. (a) On the left, the f-kdomain are displayed with the superimposition of the maxima of the spectral density (magenta dots for main maxima, white dots for local maxima). Power spectrum density scale in V^2/Hz. (b) On the right, the dispersion curves inferred from f-k maxima: red and blue dots correspond to absolute and local maxima, respectively.*

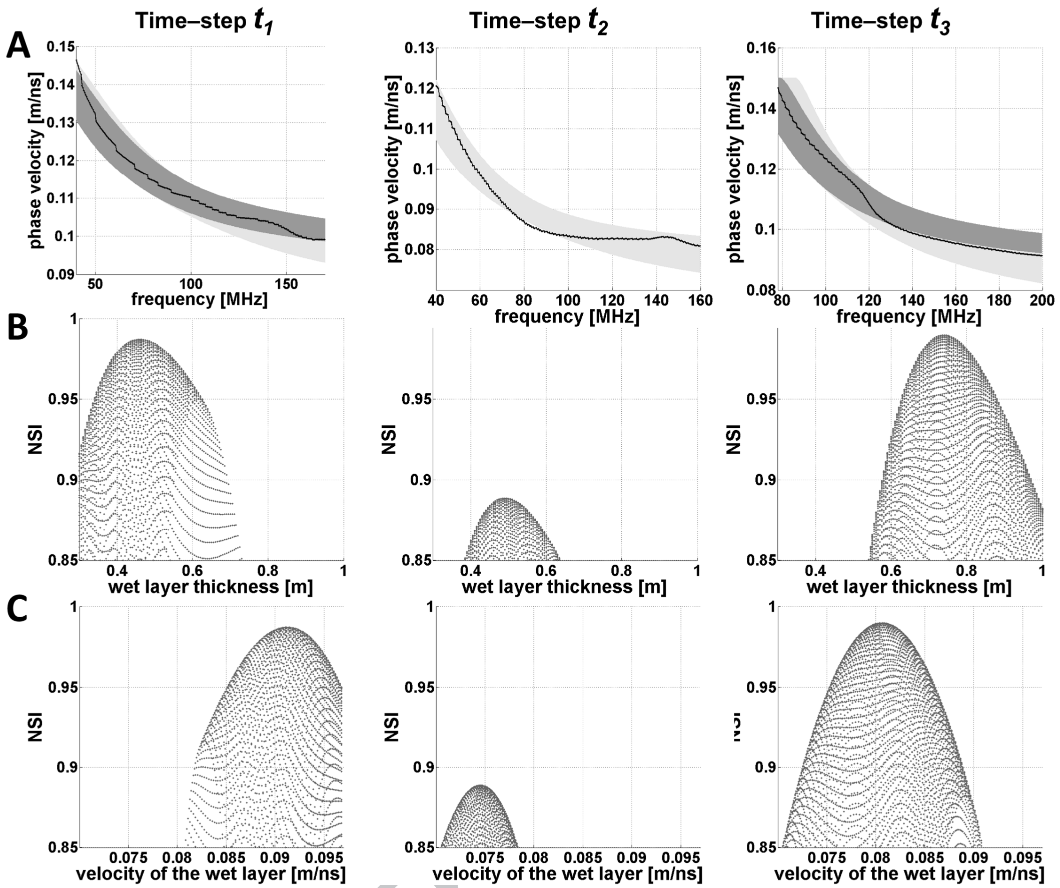

Figure 5. *Parameterizations of the simulations of slab waveguides that best fit the measured dispersion curves. (a) Superposition of the field-derived dispersion curves (black dotted lines)and of the best simulated dispersion curves: light gray lines with 0.85<NSI>0.95 and dark gray lines with NSI>0.95. (b) Wet layer thickness from the best simulations plotted against NSI>0.85. (c) Wet layer velocity from the best simulations plotted against NSI>0.85.*

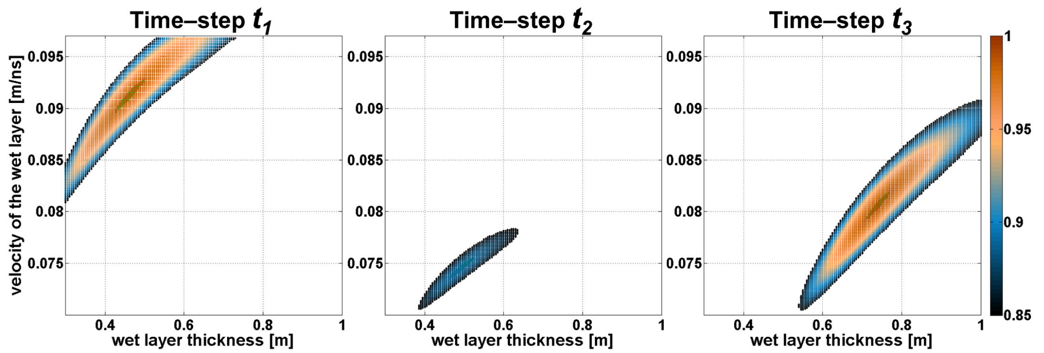

Figure 6. *Correlation between the simulated parameters: velocity and thickness of the layer that guides EM waves; color bar is NSI value. Green polygon highlights the simulations with highest NSI values for each time-steps: NSI>0.984 for* t_1, *NSI>0.886 for* t_2, *NSI>0.987 for* t_3.

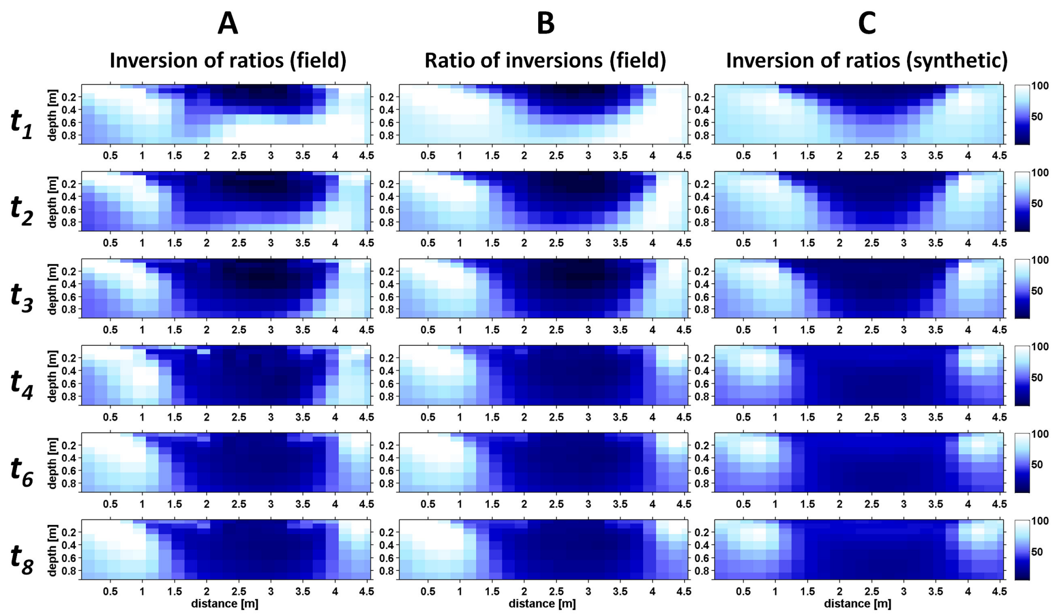

Figure 7. *Time-lapse of inverted electrical resistivity profiles displayed as percentage of variation respect to background. A) Inversion of the ratio of apparent resistivities, measured at the field, respect to background survey. B) Ratio of the inverted profiles related to background inversion. C) Inversion of the ratio of synthetic apparent resistivities, simulated through the hydrological model, respect to the assumed homogeneous background state.*

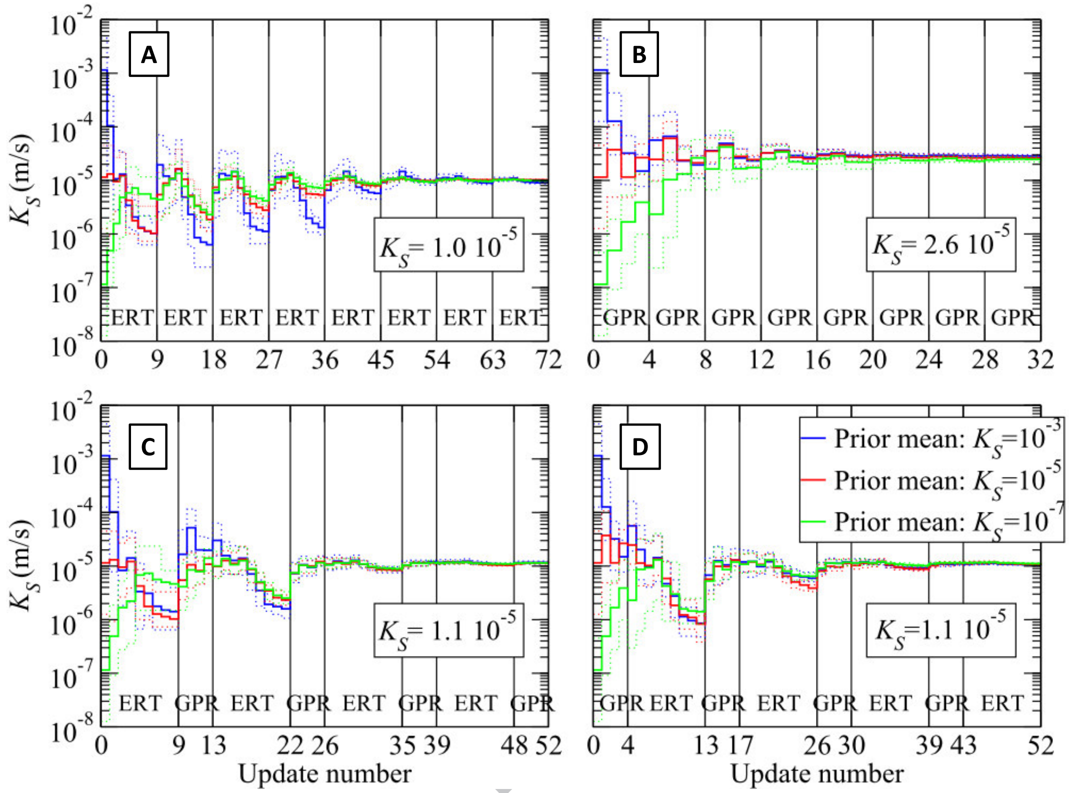

Figure 8. $\boldsymbol{K_s}$*-distributionduring the iteration of the data assimilation framework. The lines of different colors (blue, red and green) point out different initial distribution of the parameter: solid line is the mean of the distribution, dashed lines are the maximum and minimum vales in the range. (a) sequential assimilation of the ERT data. (b) sequential assimilation of the waterfront position from GPR data. (c) sequential assimilation of ERT and GPR information. (d) sequential assimilation of GPR and ERT information. The vertical lines, including the graph extremes, indicate the 9 measurement instants (t_0 to t_8).*

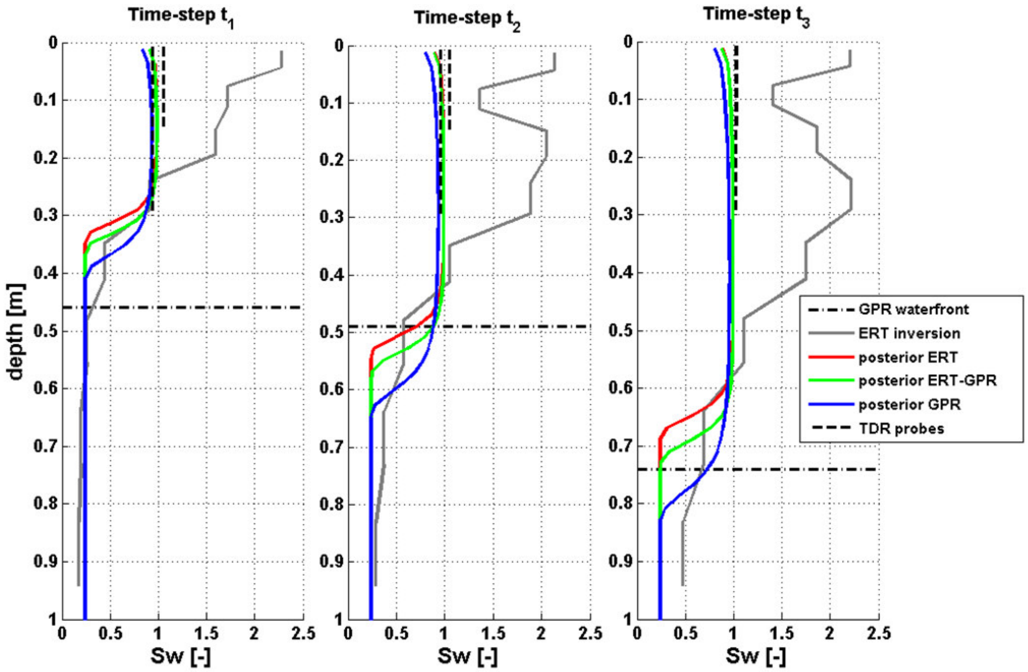

Figure 9. *Vertical profiles of water saturation, extrapolated on the position of the sprinklers line. Solid lines of red, blue and green colors are the results of forward hydrological models obtained with the* $\boldsymbol{K_s}$ *estimation assimilating only ERT, only GPR and both techniques, respectively. Gray solid line is the result of the uncoupled ERT inversion. The horizontal black dot-dashed line is the estimation of waterfront location from GPR-EM-waveguide inversion. The vertical black dashed lines are the estimated water saturation achieved by TDR probes (15 and 30 cm length).*

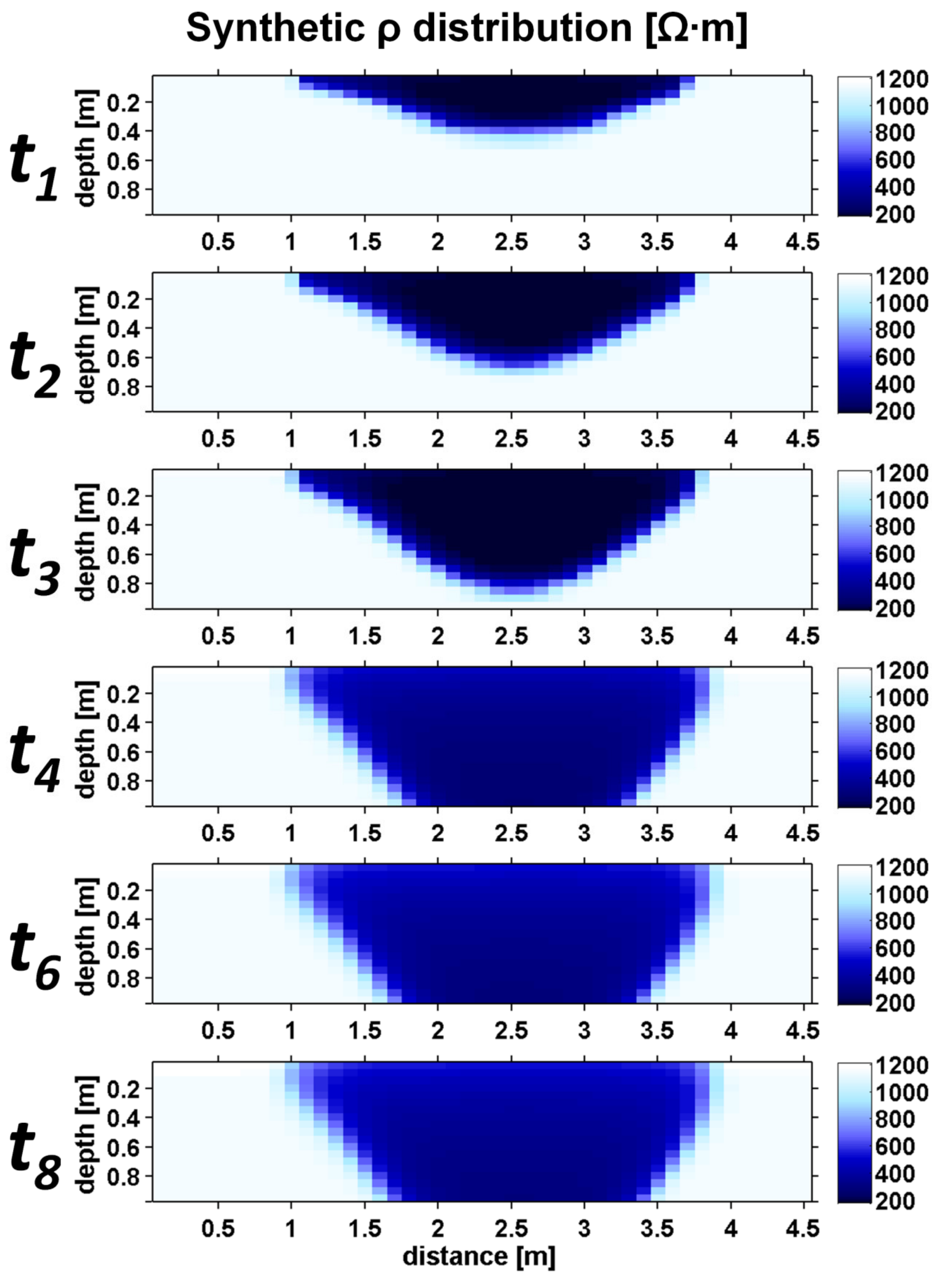

1092

1093 **Figure 10.** *Electrical resistivity sections at different time steps, derived by the*
1094 *hydrological model inferred from the assimilation of both ERT and GPR datasets.*